2024 IEEE/RSJ International Conference on Intelligent Robots and Systems (IROS)
October 14-18, 2024. Abu Dhabi, UAE

Static Modeling of the Stiffness and Contact Forces of Rolling Element Eccentric Drives for Use in Robotic Drive Systems

Simon Fritsch[1], Stefan Landler[1], Michael Otto[1], Birgit Vogel-Heuser[2], *Fellow, IEEE*, Markus Zimmermann[3], and Karsten Stahl[1]

***Abstract*— Rolling element eccentric drives promise to be an easy-to-manufacture and performant gear system for robotic actuators. They share characteristics with other eccentric drives, such as strain wave and cycloidal drives, but use rolling elements instead of an eccentric gear. They offer reduced manufacturing complexity and costs by using readily available standard parts. Little research into rolling element eccentric drives is available, and their characteristics are still underexplored. This work uses a contact-based model to investigate the previously unknown stiffness of rolling element eccentric drives. Such calculation methods are well established for structurally similar components, such as cycloidal drives and roller bearings, and provide a high-level and computationally efficient model. Good stiffness models are critical for accurately predicting robotic actuator behavior and enabling better control of robotic systems. Additionally, the proposed model is used to calculate the contact forces under load occurring in rolling element eccentric drives. Contact forces are critical to calculating a drive's load capacity, lifetime, and efficiency and serve as the foundation for further research. The mathematical description of the proposed model is derived, and the stiffness of a representative rolling element eccentric drive is calculated. Different manufacturing techniques, characterized by tolerance levels and material choices, are compared. Irrespective of manufacturing precision, similar stiffness curves result for drives made of steel, but higher contact forces result from less precise manufacturing. The stiffness of drives made from 3D printed plastic is considerably lower than that of drives made from steel. Additionally, the stiffness of rolling element eccentric drives is compared to similar eccentric drives, and a comparable twist-over-torque curve is shown.**

I. Introduction

Drive systems are of high importance for robotics. They have a major impact on robotic systems' payload capacity, performance, and price [1]. Typical robotic drive systems employ a high-ratio gearbox to reduce the speed and increase the torque of an electric motor. For this application, eccentric drives, such as cycloidal and strain wave drives, are particularly important [2]–[4].

In a previous work [5], a variant of eccentric drives utilizing rolling elements was discussed. Rolling Element Eccentric (REE) drives promise easier manufacturability than other eccentric drives while maintaining their benefits, such as high transmission ratios and stiffness.

REE drives are of interest for homemade and lightweight robots because they can be manufactured using 3D printing and composite construction techniques utilizing standard parts. In contrast, strain wave drives present major challenges for low-cost manufacturing and 3D printed cycloidal drives need additional metal components due to the required output pins [6]. Fig. 1 shows previously constructed prototypes which were 3D printed using the Fused Filament Fabrication (FFF) process. These prototypes show good transmission characteristics and low friction while maintaining a low weight and low cost.

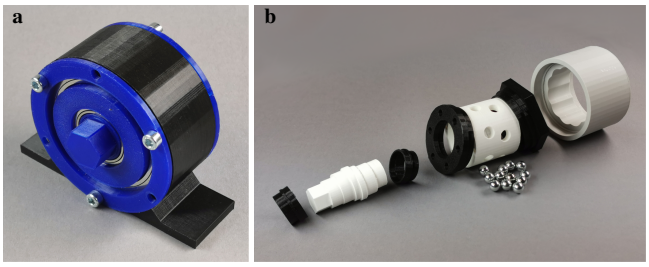

Fig. 1. Assembled 3D printed REE drive prototype (a) and disassembled 3D printed parts and rolling elements (b). (Reprinted from [5] under CC BY 4.0)

Due to the lack of research into REE drives, their precise characteristics are still unknown. This work proposes a simulation approach for REE drives based on contact deformations. Contact-based models are well established for cycloidal drives [7], [8] and roller bearings [9], enabling easier-to-implement and faster calculations than FEM-based approaches.

In this work, the proposed simulation model is used to calculate the stiffness and backlash of REE drives. The stiffness curves resulting from different manufacturing techniques are computed, and the results are compared to established cycloidal and strain wave drives.

Stiffness and backlash are central issues in robotic actuation [10]. Depending on the task, either a high or a low stiffness actuator may be preferable [11], but nearly all robotic applications benefit from accurate stiffness models. Consequentially, establishing such a model is a key step towards the adoption of REE drives in robotics.

An accurate stiffness and contact force model is critical to predicting the performance of a robotic gear system [12]. This work is part of the project DSL4RAS [1], which uses an

Research based on project 461993234, which is supported by the German Research Foundation (DFG).

All authors are with Technical University of Munich, Germany; TUM School of Engineering and Design, Department of Mechanical Engineering; Munich Institute of Robotics and Machine Intelligence (MIRMI).

Simon Fritsch is the corresponding author (Email: simon.fritsch@tum.de).

[1] Institute of Machine Elements, Gear Research Center (FZG).

[2] Institute of Automation and Information Systems (AIS).

[3] Laboratory for Product Development and Lightweight Design (LPL).

interdisciplinary approach including a description language [13] in order to model and predict robot-like systems in real-life environments. Stiffness is not only a criterion for actuator performance but also has uses in the modeling and control of robotic systems. An accurate stiffness model can increase the accuracy of position and force control of robotic systems [11], [14].

Additionally, the proposed simulation model is used to calculate the load distribution and contact forces of REE drives. Such calculations serve as a foundation for further investigations. Knowledge of the occurring contact forces is essential in order to investigate the load capacity, lifetime, and efficiency of REE drives. This allows for comparisons between different designs and enables an optimization of the drive geometry ahead of an experimental investigation. Without such an optimization, an experimental drive may not accurately reflect the capabilities of REE drives.

II. State of the Art

The overall structure of a REE drive is shown in Fig. 2. The shown drive has a crank-to-cage transmission ratio of 10 and uses two eccentricities offset by 180°. REE drives work by pushing rolling elements into an outer ring gear by means of an eccentric crank. The gear geometry transforms the radial movement of rolling elements into tangential movement, which is constrained by the cage. In order to use a REE drive as a reducer, the crank must be used as the input, and the gear or the cage can be used as the output, with the other providing a fixed reference. [5]

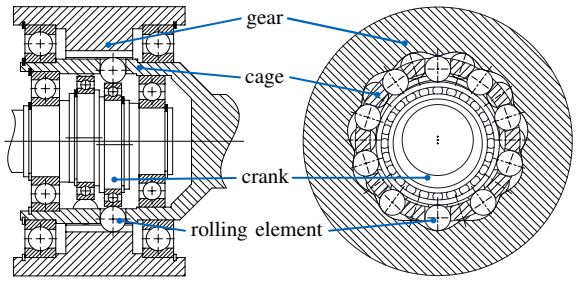

Fig. 2. Structure and components of a rolling element eccentric drive. (Adapted from [5] under CC BY 4.0)

Different kinds of rolling elements can be used in REE drives. The choice in rolling element and several further design choices are discussed in [5].

REE drives promise easier manufacturability due to their use of standard parts. Both the rolling elements and the bearings used as the crank surface are readily available and precise standard parts. If spherical balls are used as the rolling element, the cage can be easily manufactured using turning and cross-drilling [5]. This leaves only the gear geometry as a complication, which can be fabricated using CNC milling or additive manufacturing. In contrast, strain wave and cycloidal drives require multiple complex parts, which lead to higher costs and make custom drives difficult.

This work uses the nomenclature established in [5]. Fig. 3 shows an overview of the underlying geometry. The path of the rolling elements is described by the distance c parametrized as a function of the angle β. The gear geometry is formed by an equidistant of the rolling elements path. The gear geometry is parametrized in terms of β and is 2π-periodic. Tolerances can be included by adjusting the distance of the equidistant q. For a detailed derivation of the gear geometry, see [5].

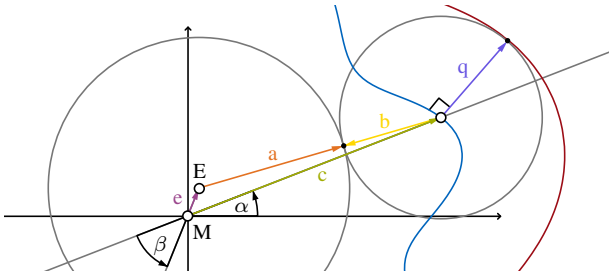

Fig. 3. Underlying geometry of REE drives. The path of the rolling elements is shown in blue, and the resulting gear geometry is shown in red. (Adapted from [5] under CC BY 4.0)

No previous works on the stiffness or contact forces of REE drives are known to the authors. However, there are several works on the stiffness and contact forces of other robotic gear systems that can serve as a reference for REE drives. Modern robotics predominantly use strain wave, planetary, and cycloidal drives [2], [3], [10].

Strain wave drives, also known under the brand name ”Harmonic Drive,” use a deformable flex spline meshing with an outer ring gear. The flex spline is elastically deformed by an eccentric wave generator [15]. Due to the elastic deformation of the flex spline, analytical approaches are limited, and FEM simulations have established themselves as the state of the art [16], [17]. The deformation behavior central to strain wave drives does not occur in REE drives, and methods established for strain wave drives are limited in their transferability.

Planetary gear systems use a number of gears revolving around a central sun gear and meshing with an outer ring gear to transmit torque. Several kinematic variations of this principle are established [18] but all share in common that their stiffness is dominated by tooth contacts and deformations [10]. Involute teeth are thinner and more prone to bending than the cycloidal-like teeth of REE drives. Consequentially, calculation methods established for planetary gearsets are not easily transferable to REE drives.

Cycloidal drives employ cam discs mounted on an eccentric crank to transmit torque. The cam discs mesh with an outer pin wheel consisting of regularly spaced cylindrical pins. The resulting eccentric motion of the cam discs is converted into a rotary output using pin rollers [19]. The stiffness of cycloidal drives is dominated by the stiffness of the occurring contacts. Consequentially, contact-based simulation models for the stiffness and contact forces of cycloidal drives are well established and represent an alternative to FEM simulations [7], [8].

Cycloidal drives share many similarities with REE drives. The totality of rolling elements in a REE drive can be equated to the cycloidal cam of a cycloidal drive. Additionally, the resulting gear geometry of a REE drive is similar to a cycloidal curve [5]. These similarities suggest that calculation models for cycloidal drives could be transferred to REE drives.

Additionally, the structural similarity between REE drives and roller bearings can be noted [5]. Contact-based calculation models are the state of the art for calculating the stiffness and load distribution of roller bearings, as described in standards for the calculation of roller bearing properties [9]. These models can serve as a reference for REE drives.

The stiffness and backlash of gear systems can be expressed as a twist-over-torque curve. A drive's backlash is expressed as a steep change in twist angle under negligible load. The stiffness of the drive is expressed as the derivative of the curve. [10]

III. Simulation Approach

The stiffness of REE drives is modeled using a contact-based approach. Deformations outside the contact are neglected based on similar works for cycloidal drives [7]. Each rolling element is modeled separately. The cage and gear are fixed, and the crank is twisted relative to the neutral position. The static equilibrium position of a rolling element is calculated for different crank angles of twist ϕ. The output torque resulting from one rolling element at a given angle of twist ϕ and point on the gear profile, determined by the angle β, can be calculated from the contact forces. The total output torque for different angles of twist can then be calculated by adding the contributions of the individual rolling elements.

All relevant displacements and forces occur in a two-dimensional plane orthogonal to the axis of rotation. Consequentially, the position of the rolling element and crank and the occurring forces are modeled in two dimensions. The position of the rolling element $\mathbf{x}$ is tracked using a local coordinate system centered on the neutral position of the rolling element. The basis vectors of this coordinate system point in the radial and tangential directions. The configuration of the drive in the neutral (grey) and a twisted (blue) position are shown in Fig. 4.

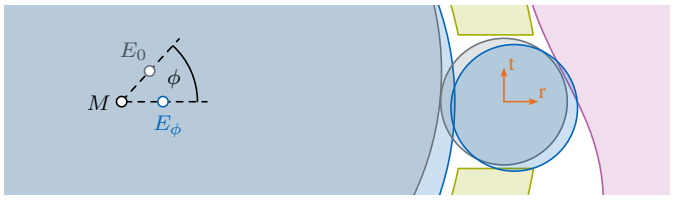

Fig. 4. Neutral (grey) and twisted (blue) position of the drive around one rolling element. The positions of the local coordinate system (orange), cage (green), and gear (purple) are independent of the angle of twist ϕ. The center of rotation of the drive M, the neutral center of the eccentricity E_0, and the twisted center of the eccentricity E_ϕ are marked.

Four contact points occur in the considered plane:

- C_1 Rolling Element - Ring Gear
- C_2 Rolling Element - Eccentric Crank
- C_3 Rolling Element - Cage t+
- C_4 Rolling Element - Cage t-

Fig. 5 shows the contact points for one rolling element. The crank is shown in blue, the cage is shown in green, and the gear is shown in purple.

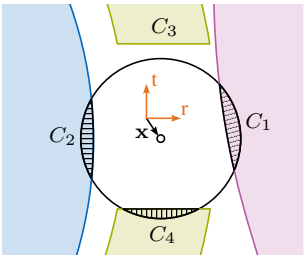

Fig. 5. Contact points and overlap of one rolling element at position $\mathbf{x}$. No overlap results for C_3.

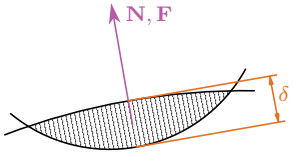

Fig. 6. Relative indentation δ, normal vector $\mathbf{N}$, and resulting force vector $\mathbf{F}$ of one contact.

The deformation at each contact is modeled using a purely elastic contact model. The contact force F_N can be expressed as a generalized equation depending on the relative indentation δ and two contact stiffness parameters K and n [20]:

$$F_N = K\,\delta^n. \tag{1}$$

The exponent n depends on the geometry of the contact. Line contact resulting from cylindrical rollers and point contact resulting from spherical rollers lead to different exponents n. The factor K depends on the radii and material properties of the elements in contact. It is constant for contacts C_2, C_3, and C_4. For the contact with the gear C_1, K depends on the point of contact with the gear due to its variable radius:

$$K_1 = f(\beta), \qquad K_2,\, K_3,\, K_4 = const. \tag{2}$$

For negative relative indentations $\delta < 0$, no contact occurs. This is modeled using the Heaviside function $\sigma(\delta)$:

$$F_N = K\,\delta^n\,\sigma(\delta)\,. \tag{3}$$

The force vector $\mathbf{F}_j$ corresponding to an individual contact C_j is given by the product of the normal force $F_{N,j}$ and normal vector $\mathbf{N}_j$:

$$\mathbf{F}_j = K_j\,{\delta_j}^n\,\sigma(\delta_j)\,\mathbf{N}_j\,. \tag{4}$$

The parameters of the contact model can be chosen based on the geometry of the contacts and modeling assumptions. For the contact model used in this work, see Section IV.

The normal vectors $\mathbf{N}_j$ and the relative indentations δ_j of the contacts can be calculated based on the drive's geometry and are independent of the chosen contact model. By convention, the normal vectors are oriented to point toward the center of the rolling element, i.e., in the direction of the forces acting on the rolling element. Fig. 6 shows one contact's relative indentation, normal vector, and force vector. The properties of each contact are calculated based on the radii r_{RE}, r_{Crank}, and r_{Cage} as well as the distance of the equidistant q. These quantities include tolerances.

The contact C_1 is simplified by linearizing the relative indentation δ_1 and assuming a constant stiffness parameter K_1 for each point on the gear profile. These assumptions hold for small displacements $\mathbf{x}$ of the rolling element but become increasingly inaccurate for larger displacements. The normal vector of the gear calculated in [5] was rotated into the local coordinate system. For ease of notation, the radial component n_r and the tangential component n_t of the non-normalized normal vector are calculated separately:

$$n_r = z^{-1} c\,. \tag{5}$$

$$n_t = e\sin(\beta)\left(1 + \frac{e\cos(\beta)}{\sqrt{(a+b)^2 - e^2\sin^2(\beta)}}\right). \tag{6}$$

The inwards pointing, unit normal vector $\mathbf{N}_1$ is given by:

$$\mathbf{N}_1 = \frac{1}{\sqrt{n_r^2 + n_t^2}}\begin{bmatrix} -n_r \\ -n_t \end{bmatrix}. \tag{7}$$

The relative indentation δ_1 can be calculated by projecting the position of the rolling element $\mathbf{x}$ along the normal vector N_1 and offsetting the result rolling elements radius r_{RE} and the distance of the equidistant q:

$$\delta_1 = r_{RE} - q - \mathbf{N}_1 \cdot \mathbf{x}\,. \tag{8}$$

The contact between the crank and the rolling element C_2 happens between two circular cross-sections. The connecting line $\mathbf{d}$ from the center of the eccentricity to the center of the displaced rolling element is given by:

$$\mathbf{d} = e\begin{bmatrix} -\cos(\beta+\phi) \\ -\sin(\beta+\phi) \end{bmatrix} + c\,(\beta)\begin{bmatrix} 1 \\ 0 \end{bmatrix} + \mathbf{x}\,. \tag{9}$$

The relative indentation δ_2 can be obtained by subtracting the magnitude of $\mathbf{d}$ from the sum of the radius of the rolling element r_{RE} and the radius of the crank r_{Crank}:

$$\delta_2 = r_{RE} + r_{Crank} - ||\mathbf{d}||\,. \tag{10}$$

The unit normal vector $\mathbf{N}_2$ can be computed by normalizing $\mathbf{d}$:

$$\mathbf{N}_2 = \frac{\mathbf{d}}{||\mathbf{d}||}\,. \tag{11}$$

In the modeled plane, two contact points can occur between the rolling element and the cage bore. The contact in the positive tangential direction is called C_3, and the contact in the negative tangential direction is called C_4. The normal vectors of both contacts are oriented towards the origin of the local coordinate system and have no radial component:

$$\mathbf{N}_3 = \begin{bmatrix} 0 \\ -1 \end{bmatrix}, \quad \mathbf{N}_4 = \begin{bmatrix} 0 \\ 1 \end{bmatrix}. \tag{12}$$

The distance between the neutral position of the rolling element and the cage walls, including tolerances, is called the radius of the cage r_{Cage}. For spherical rolling elements, this is equivalent to the radius of the cage bore. The relative indentation of contacts C_3 and C_4 can be expressed in terms of the tangential component of the rolling elements position x_t, the rolling elements radius r_{RE} and the radius of the cage r_{Cage}:

$$\delta_3 = x_t + r_{RE} - r_{Cage}\,. \tag{13}$$

$$\delta_4 = -x_t + r_{RE} - r_{Cage}\,. \tag{14}$$

The total force acting on one rolling element $\mathbf{F}_{total}(\mathbf{x})$ is given by the sum of the contact force vectors $\mathbf{F}_j$:

$$\mathbf{F}_{total}(\mathbf{x}) = \sum_{j=1}^{4}\mathbf{F}_j = \sum_{j=1}^{4} K_j\ (\delta_j(\mathbf{x}))^n\,\sigma(\delta_j(\mathbf{x}))\,\mathbf{N}_j\,. \tag{15}$$

The resulting vector field represents the total force acting on one rolling element. Additional forces, such as gravitational or dynamic influences, can be added to this sum but are disregarded in this work. At the static equilibrium, all forces acting on the rolling element must cancel out, i.e., the total force must be $\mathbf{0}$. This results in an implicit equation for the static equilibrium position of the rolling element $\mathbf{x}_{stat}$:

$$\mathbf{F}_{total}(\mathbf{x}_{stat}) \stackrel{!}{=} \mathbf{0}\,. \tag{16}$$

This equation can be solved for $\mathbf{x}_{stat}$ using numerical methods. In general, the resulting solutions are not unique due to the tolerances of the parts. Non-unique solutions occur when the rolling element has play and are irrelevant to the drive's torque generation, stiffness, and contact forces.

The force vector field is conservative, as it is the gradient of the stored energy. This enables gradient descent to be used to find solutions. Alternatively, non-linear equation solvers can be used. For these, it is advantageous to explicitly calculate the Jacobian matrix of the force $\mathbf{F}_{total}(\mathbf{x})$. The Heaviside function is defined such that the root of the normal force compensates its non-differentiability at 0. The Jacobian of the total force is given by:

$$\mathbf{J}(\mathbf{x}) = \left(\sum_{j=1}^{4} -K_j\,\sigma(\delta_j)\,n\,{\delta_j}^{n-1}\,\mathbf{N}_j \otimes \mathbf{N}_j\right) + K_2\,\sigma(\delta_2)\,{\delta_2}^n\,\nabla\mathbf{N}_2\,. \tag{17}$$

In this equation, the tensor product $\otimes$ is equivalent to the outer product of the vectors. The Jacobian of $\mathbf{N}_2$ is given by:

$$\nabla\mathbf{N}_2 = ||\mathbf{d}||^{-1}\left(\begin{bmatrix} 1 & 0 \\ 0 & 1 \end{bmatrix} - \sqrt{2}\ \mathbf{N}_2 \otimes \begin{bmatrix} \sqrt{d_r} \\ \sqrt{d_t} \end{bmatrix}\right) \tag{18}$$

with d_r and d_t as the radial and tangential component of the vector $\mathbf{d}$. Using this explicitly calculated Jacobian matrix increases the computation speed of the solver considerably.

The output torque resulting from one rolling element for a given twist angle ϕ can be calculated using its static equilibrium position and the corresponding contact forces. The drive's output torque is given by the product of the rolling element's leverage times the resulting force on the cage. The rolling element's leverage is given by the sum of the path distance c and radial component of the rolling element's static equilibrium position $x_{stat,r}$. The force on the

cage is given by the difference between the normal forces resulting from contacts C_3 and C_4:

$$T_{out} = (c + x_{stat,r}) \left(F_{N,3} \left(\mathbf{x}_{stat} \right) - F_{N,4} \left(\mathbf{x}_{stat} \right) \right) . \quad (19)$$

The total output torque of the drive at a given angle of twist is calculated using a Monte-Carlo simulation to account for random tolerance variations. Tolerances are modeled as normal distributions centered on the specified tolerance range. The standard deviation of this distribution is chosen such that the specified tolerance limits lie at three standard deviations from the mean. This results in $99.7\,\%$ of parts lying in tolerance. Furthermore, it was assumed that the tolerances of different rolling elements and parts are statistically independent and that no systematic error affects them.

A number of rolling elements with randomly determined tolerances are simulated. The total number of simulated rolling elements n_{RE} can be arranged on a single eccentricity or on multiple offset eccentricities. See [5] for additional considerations regarding the number and arrangement of eccentricities. The position of the initial rolling element β_0 is determined randomly using a uniform distribution from 0 to 2π. All further rolling elements are spaced evenly on the gear profile:

$$\beta_k = \beta_0 + k \, \frac{2\pi}{n_{RE}} , \qquad \forall \, k = 0, 1, \ldots , n_{RE} . \quad (20)$$

The static equilibrium position, contact forces, and output torques of these rolling elements are then calculated over a range of twist angles. Additional attention must be paid if the gear geometry is self-intersecting. Any rolling elements in the self-intersecting portion of the gear must be excluded from this calculation as they are incapable of generating torque. The total output moment $T_{out,total}(\phi)$ is given by the sum of the individual contributions of the rolling elements:

$$T_{out,total}(\phi) = \sum_{k=1}^{n_{RE}} T_{out,k}(\phi) . \quad (21)$$

This simulation is repeated multiple times with different randomly generated tolerances in order to obtain statistical data about the drive's performance.

IV. Simulated Drive and Simulation Parameters

The simulation approach described in Section III was used to investigate the stiffness of a representative REE drive. A drive using spherical rollers on three eccentric cranks offset by 120° was chosen based on the considerations described in [5] and available cycloidal drives [21]. The base dimensions of the chosen drive are listed in Table I. A comparison of different REE drive geometries and transmission ratios is beyond the scope of this work.

Different variants of this drive were simulated to investigate the effect of manufacturing techniques on REE drives. All simulated drives use steel balls as rolling elements and a steel bearing as the crank due to their availability, low price, and high precision. Balls with a tolerance class of G10 according to ISO 3290 [22] and a bearing with a tolerance class of "Normal" according to ISO 492 [23] were chosen for all drives. The tolerances of the cage and gear were based on the state of the art for the chosen manufacturing techniques [24]–[28] and denoted using the tolerance grades defined in ISO 286 [29]. The manufacturing techniques, tolerance grades, tolerance windows for the diameters, and standard deviations of the radii are denoted in Table II.

TABLE I

Geometry and dimensions of the simulated REE drives.

Dimension	Chosen Value
Radius of the crank a	$41\,\mathrm{mm}$
Radius of the rolling element b	$7\,\mathrm{mm}$
Eccentricity of the crank e	$0.7\,\mathrm{mm}$
Transmission ratio from the crank to the cage i	29
Total number of rolling elements n_{RE}	87

TABLE II

Tolerances of the simulated REE drives.

Component	Tolerance Grade	Diameter Tolerance	Standard deviation of the radius
All Drives			
Radial bearing used as the crank surface	ISO 492 Normal	$13\,\mu\mathrm{m}$	$1.08\,\mu\mathrm{m}$
Ball used as the rolling element	ISO 3290 G10	$0.5\,\mu\mathrm{m}$	$0.042\,\mu\mathrm{m}$
Drive 1			
Ground gear profile	IT 5	$15\,\mu\mathrm{m}$	$1.25\,\mu\mathrm{m}$
Honed cage bore	IT 4	$5\,\mu\mathrm{m}$	$0.42\,\mu\mathrm{m}$
Drive 2			
Milled gear profile	IT 9	$87\,\mu\mathrm{m}$	$7.25\,\mu\mathrm{m}$
Reamed cage bore	IT 6	$11\,\mu\mathrm{m}$	$0.92\,\mu\mathrm{m}$
Drive 3			
FFF 3D printed gear	IT 11	$220\,\mu\mathrm{m}$	$18.33\,\mu\mathrm{m}$
FFF 3D printed cage bore	IT 13	$270\,\mu\mathrm{m}$	$22.5\,\mu\mathrm{m}$

The mean deviation of the crank radius, rolling element radius, and gear equidistant were chosen to be 0 in order to avoid backlash. The mean radius of the cage bore was chosen to be three standard deviations larger than the nominal radius in order to avoid excess friction.

All components except for the cage and gear of drive 3 were made from hardened 100Cr6 steel with a Young's modulus E of $208\,\mathrm{GPa}$ and Poisson's ratio ν of 0.30 [30]. The material properties of the drive 3's cage and gear were based on the properties of 3D printed PLA, with a Young's Modulus E of $3\,\mathrm{GPa}$ and a Poisson's Ratio ν of 0.33 [31], [32].

A Hertzian contact model based on the state of the art in roller bearings [9], [30] was chosen as the contact model. For a contact C_j between the bodies A and B the contact parameters are:

$$n = \frac{3}{2} , \quad (22)$$

$$K_j = \left(\frac{3}{4\sqrt{2}} \left(\frac{1-{\nu_A}^2}{E_A} + \frac{1-{\nu_B}^2}{E_B} \right) \sqrt{\Sigma p_j \left(\frac{\psi_j}{\xi_j} \right)^3} \right)^{-1}. \tag{23}$$

The material properties of the bodies are described by their Young's moduli, E_A and E_B, and their Poisson's ratios ν_A and ν_B. Σp_j is the curvature sum of the contact C_j. The Hertzian coefficient $\frac{\psi_j}{\xi_j}$ was interpolated between tabular data adapted from [30]. The curvature sums Σp_j and Hertzian coefficients $\frac{\psi_j}{\xi_j}$ were calculated based on the radii of the parts, including tolerances.

The local radius of curvature of the gear was calculated by using symbolical differentiation to determine the curvature of the rolling elements path $\mathbf{c}$. To this, the distance of the equidistant q was added. Due to the concave nature of the gear, the negative of this radius must be used according to the conventions for Hertzian contacts:

$$\mathbf{c}(\beta) = c(\beta) \begin{bmatrix} \cos(z^{-1}\beta) \\ \sin(z^{-1}\beta) \end{bmatrix}. \tag{24}$$

$$r_{Gear} = -\left(\frac{||\mathbf{c}'||^3}{\det(\mathbf{c}', \mathbf{c}'')} + q \right). \tag{25}$$

For each variant, 1000 full drives were simulated, resulting in 87 000 simulated rolling elements per variant.

V. Results

Three different REE drives were simulated, and their twist-over-torque curves were calculated. Fig. 7 shows the resulting mean twist-over-torque curves and the 10th and 90th percentile of the generated torque for each twist angle. It can be observed that the mean twist-over-torque curves of the metal drives, drive 1 (blue) and drive 2 (orange), are similar and overlap each other. Drive 3 (purple) shows a considerably lower stiffness and consequentially higher twist angles at the same torque.

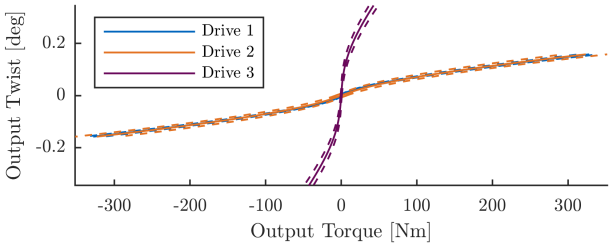

Fig. 7. Twist-over-torque curves of the simulated drives. Solid lines show the mean generated torque of the simulated drives. Dashed lines show the 10th and 90th percentile of the generated torque. Drive 1 (blue) and 2 (orange) overlap, reducing the visibility of drive 1.

It should be noted that the limits of the simulated torques do not equate to the torque ratings of the drives. The range of simulated twist angles was limited based on the occurring pressures, but no in-depth calculation of the maximum torque for the drives was performed. An in-depth investigation into the permissible torques of REE drives is subject to future research.

Additionally, the simulated stiffness of REE drives was compared to other eccentric drives. A strain wave drive and a cycloidal drive with similar outer diameters and transmission ratios were chosen for this comparison. Harmonic drive's "HFUS-40-2A" [33] with a transmission ratio of 50 was chosen as a representative strain wave drive. Sumitomo's "Fine Cyclo F1C-A 25" [21] with a transmission ratio of 29 was chosen as a representative cycloidal drive. The published specifications were used to calculate the twist-over-torque curves of these drives.

Fig. 8 shows the mean twist-over-torque curve of REE drive 1 (blue) compared to the chosen strain wave drive (green) and cycloidal drive (yellow). Drive 1 was selected for the comparison because it represents the manufacturing techniques and materials used in the chosen strain wave and cycloidal drive. The REE drive has a slightly lower stiffness than the established eccentric drives.

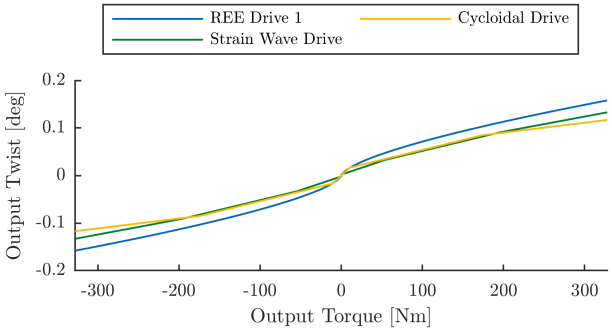

Fig. 8. Mean twist-over-torque curves of the simulated REE drive 1 and the chosen strain wave and cycloidal drive. Harmonic drive's "HFUS-40-2A" [33] with a transmission ratio of 50:1 was chosen as the strain wave drive. Sumitomo's "Fine Cyclo F1C-A 25" [21] with a transmission ratio of 29:1 was chosen as the cycloidal drive.

Additionally, the contact forces of all rolling elements were computed. The maximum normal forces at each contact point were calculated for each simulated drive. The results are shown in Fig. 9. It can be observed that the larger tolerances of drive 2 lead to higher and more variable contact forces compared to drive 1. Due to the chosen tolerance fields, drive 2 and drive 3 also show substantial contact forces when no twist, and with it no load, is present. Furthermore, the occurring contact forces of drive 3 are considerably lower than those of the drives manufactured from metal. Additionally, the load distribution was visualized by dividing the highest torque contribution of a given drive's rolling elements by the total output torque of the drive. The resulting load shares are shown in Fig. 10. Load shares at low torques are not representative due to random variations in the part tolerances and are excluded. It can be observed that the load shares start high for low loads and asymptotically approach a value between 10 % and 20 % for high loads. In other words, around 10 % to 20 % of the drive's output torque is transmitted by a single rolling element during increased loads. Additionally, the load share of drive 1 is lower than the load shares of drive 2 and 3, and less deviation occurs as the result of random variations.

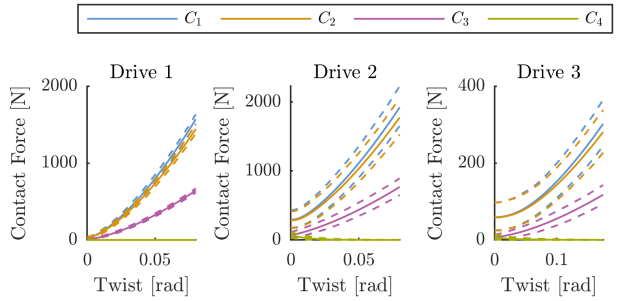

Fig. 9. Maximum contact forces of the simulated drives. Dashed lines indicate the 10th and 90th percentile of simulated drives.

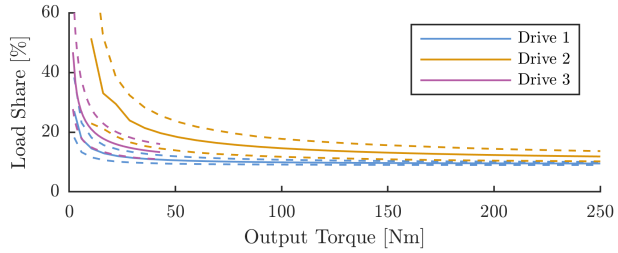

Fig. 10. Load distribution of the simulated drives. The load share is defined as the maximum torque contribution of a rolling element divided by the total output torque of the drive. The low torque region, which is strongly affected by random variations, is excluded. Dashed lines indicate the 10th and 90th percentile of simulated drives.

VI. Discussion

The simulated performance of the REE drives matches the expected results. The overall shape of the twist-over-torque curves matches the chosen comparisons and published research. The slightly lower stiffness of the simulated REE drive compared to the published specifications of other eccentric drives can be explained by the difference between point and line contact. The point contact of the simulated REE drive leads to a fundamentally lower stiffness than the line contact of the chosen cycloidal and strain wave drive [20]. A high-stiffness line contact can be realized by choosing cylindrical rollers instead of balls.

The increased contact forces under no load of drives 2 and 3 are expected to cause higher friction during load-free operation. These contact forces are caused by the mean value of the chosen tolerance fields and could be reduced by choosing a tolerance field with less overlap. In turn, such a tolerance field reduces the drive's stiffness in the no-load region. Decreasing the overlap even further could fully eliminate these forces at the cost of introducing backlash into the drive. This trade-off between stiffness/backlash and friction in the no-load region must be considered during the design of a REE drive. As demonstrated by drive 1, more precise manufacturing techniques decrease the necessity of such a trade-off. In turn, such drives are more difficult and more expensive to fabricate.

The contact forces of drive 3 are considerably lower than the other drives because the plastic material used for them is less stiff. At the same displacement, less force occurs, leading to the lower output torque and stiffness of the 3D printed drive.

The load distribution of the drive is affected by the occurring pressure angles of the gear. Close to the peaks and troughs, the gear's pressure angle γ approaches 0 [5], and no torque can be generated. Consequentially, the rolling elements in the middle of the gear profile contribute the greatest amount of torque to the total output. The load share is initially higher because tolerances have a more substantial effect during low deformations. Under higher loads, the effect of tolerances decreases, and the load share approaches a fixed value determined by the geometry of the drive.

In theory, the stiffness curve of REE drives could also be obtained using a FEM approach. However, FEM requires knowledge of implementation-specific details which are unavailable in the preliminary design phase. Additionally, FEM requires considerably more computation and work to set up, which reduces the number of different drives that can be simulated. Furthermore, the high number of occurring contacts presents a challenge for finite element analysis. For the drive simulated in this work, at least 261 individual contact points occur simultaneously, with even more contacts occurring for REE drives with higher transmission ratios. For these reasons, an analytical approach such as the one outlined in this work is preferable during the current design stage.

The proposed simulation model can serve as the basis for further investigations. Knowledge of the occurring contact forces is a prerequisite for investigations of the drive's torque capacity, expected lifetime, and efficiency. Such investigations allow for an optimization of REE drive geometry and lead to a better understanding of the technology.

Once the design of REE drives has been optimized and key influencing parameters have been identified, an experimental investigation is the next step. An optimized design better reflects the capabilities of the technology, and knowledge of key design parameters allows for conscious experimental design.

VII. Conclusion and Future Work

In this work, a simulation model for the stiffness and contact forces of REE drives was derived. The model was based on established computation methods for cycloidal drives and roller bearings and uses contact models to represent deformations in the drive.

A representative REE drive was simulated using the established simulation model, and the influence of different manufacturing techniques was investigated. The drives manufactured from steel showed similar twist-over-torque curves irrespective of the manufacturing tolerances. The simulated 3D printed drive showed considerably lower stiffness due to the used plastic material. Higher contact forces during no-load conditions were observed for drives with less precise manufacturing techniques.

The twist-over-torque curve of the simulated drives was compared to commercially available eccentric drives used in robotics, and a substantial similarity between their stiffnesses was observed.

This work contributes to the theoretical foundation needed for an experimental investigation of REE drives. As an underexplored technology, REE drives lack the established knowledge base of other drive technologies. Theoretical investigations can show key influencing parameters and generate insight into the mechanisms at play. At the current preliminary design stage, experimental investigations into REE drives lack the foundation to generate meaningful insights.

Instead of experimental validation, this work relies on well-established mechanical models, state-of-the-art methods in related technologies, and comparisons to similar drives. Further work is needed in order to optimize the design of REE drives ahead of an experimental investigation. The model outlined in this work can serve as the basis of such an optimization. Additionally, investigations into the expected lifetime, efficiency, and speed limits of REE drives can be based on the proposed simulation approach. Once these foundations have been established, an experimental investigation of REE drives is planned.

REFERENCES

[1] B. Vogel-Heuser, M. Zimmermann, K. Stahl, K. Land, F. Ocker, S. Rotzer, S. Landler, and M. Otto, "Current Challenges in the Design of Drives for Robot-Like Systems," *IEEE International Conference on Systems, Man, and Cybernetics (SMC)*, pp. 1923–1928, 2020.

[2] A.-D. Pham and H.-J. Ahn, "High Precision Reducers for Industrial Robots Driving 4th Industrial Revolution: State of Arts, Analysis, Design, Performance Evaluation and Perspective," *International Journal of Precision Engineering and Manufacturing-Green Technology*, vol. 5, no. 4, pp. 519–533, 2018.

[3] P. L. García, S. Crispel, E. Saerens, T. Verstraten, and D. Lefeber, "Compact Gearboxes for Modern Robotics: A Review," *Frontiers in robotics and AI*, vol. 7, p. 103, 2020.

[4] J. W. Sensinger and J. H. Lipsey, "Cycloid vs. harmonic drives for use in high ratio, single stage robotic transmissions," *2012 IEEE International Conference on Robotics and Automation*, pp. 4130–4135, 2012.

[5] S. Fritsch, S. Landler, M. Otto, B. Vogel-Heuser, M. Zimmermann, and K. Stahl, "Discussion of a variant of eccentric drives utilizing rolling elements," *Forschung im Ingenieurwesen*, vol. 87, no. 4, pp. 1221–1230, 2023. [Online]. Available: https://link.springer.com/article/10.1007/s10010-023-00688-1

[6] W. Roozing and G. Roozing, "3D-printable low-reduction cycloidal gearing for robotics," in *IROS 2022 Kyōto - IEEE/RSJ International Conference on Intelligent Robots and Systems*, Z. Wang, N. Ando, and N. Yamanobe, Eds. Piscataway, NJ: IEEE, 2022, pp. 1929–1935.

[7] L.-C. Chang, S.-J. Tsai, and C.-H. Huang, "Contact characteristics of cycloid planetary gear drives considering backlashes and clearances," *Forschung im Ingenieurwesen*, vol. 17, no. 6, p. 1729, 2021.

[8] S.-J. Tsai and C.-H. Huang, "A study on loaded tooth contact analysis of a cycloid planetary gear reducer considering bearing roller stiffness," *The JSME International Conference on Motion and Power Transmission (MPT), 28.02-03.03.2017, Kyoto, Japan*, 2017.

[9] *Rolling bearings: Methods for calculating the modified reference rating life for universally loaded bearings*, ISO/TS 16 281, 2018.

[10] S. Landler, R. M. Blanco, M. Otto, B. Vogel-Heuser, M. Zimmermann, and K. Stahl, "Determination of the Characteristics of Gears of Robot-Like Systems by Analytical Description of their Structure," in *2023 IEEE/RSJ International Conference on Intelligent Robots and Systems (IROS)*. IEEE, 10/1/2023 - 10/5/2023, pp. 439–445.

[11] G. Pratt, A. Wright, J. Pratt, M. Williamson, and P. Dillworth, *Stiffness Isn't Everything*, 2001.

[12] K. Ziegler, M. Volpert, M. Amm, B. Vogel-Heuser, K. Stahl, and M. Zimmermann, "MBSE Incorporating time-dependent behavior for the design of robot-like systems," *Proceedings of the Design Society*, vol. 3, pp. 2585–2594, 2023.

[13] B. Vogel-Heuser, M. Zhang, B. Lahrsen, S. Landler, M. Otto, K. Stahl, and M. Zimmermann, "SysML' – incorporating component properties in early design phases of automated production systems," *at - Automatisierungstechnik*, vol. 72, no. 1, pp. 59–72, 2024.

[14] U. Schneider, M. Momeni-K, M. Ansaloni, and A. Verl, "Stiffness modeling of industrial robots for deformation compensation in machining," in *IEEE/RSJ International Conference on Intelligent Robots and Systems (IROS), 2014*. Piscataway, NJ: IEEE, 2014, pp. 4464–4469.

[15] B. Routh, "Design aspects of harmonic drive gear and performance improvement of its by problems identification: A review," *AIP Conf. Proc.*, vol. 1943, no. 1, p. 020016, 2018.

[16] F.-E. Rhéaume, H. Champliaud, and Z. Liu, "Understanding and modelling the torsional stiffness of harmonic drives through finite-element method," *Proceedings of the Institution of Mechanical Engineers, Part C: Journal of Mechanical Engineering Science*, vol. 223, no. 2, pp. 515–524, 2009.

[17] Y.-T. Tsai and Y.-Y. Hsu, "Strength analysis and reliability evaluation for speed reducers," *IOP Conference Series: Materials Science and Engineering*, vol. 235, pp. 1–7, 2017.

[18] S. Crispel, P. L. Garcia, E. Saerens, A. Varadharajan, T. Verstraten, B. Vanderborght, and D. Lefeber, "A Novel Wolfrom-Based Gearbox for Robotic Actuators," *IEEE/ASME Transactions on Mechatronics*, vol. 26, no. 4, pp. 1980–1988, 2021.

[19] D. Yang and J. Blanche, "Design and application guidelines for cycloid drives with machining tolerances," *Mechanism and Machine Theory*, vol. 25, no. 5, pp. 487–501, 1990.

[20] M. Machado, P. Moreira, P. Flores, and H. M. Lankarani, "Compliant contact force models in multibody dynamics: Evolution of the Hertz contact theory," *Mechanism and Machine Theory*, vol. 53, pp. 99–121, 2012. [Online]. Available: https://www.sciencedirect.com/science/article/pii/S0094114X1200047X

[21] Sumitomo Drive Technologies, "Catalog Fine Cyclo E Cyclo: Zero Backlash Precision Gearboxes." [Online]. Available: https://us.sumitomodrive.com/sites/default/files/2023-07/precision-gearbox-catalog-07-2021.pdf

[22] *Rolling bearings: Balls*, ISO 3290, 2014.

[23] *Rolling bearings: Radial bearings - Geometrical product specifications (GPS) and tolerance values*, ISO 492, 2023.

[24] N. Beltrán, B. J. Álvarez, D. Blanco, Á. Noriega, and P. Fernández, "Estimation and Improvement of the Achievable Tolerance Interval in Material Extrusion Additive Manufacturing through a Multi-State Machine Performance Perspective," *Applied Sciences*, vol. 11, no. 12, p. 5325, 2021.

[25] T. Lieneke, V. Denzer, G. A. Adam, and D. Zimmer, "Dimensional Tolerances for Additive Manufacturing: Experimental Investigation for Fused Deposition Modeling," *Procedia CIRP*, vol. 43, pp. 286–291, 2016. [Online]. Available: https://www.sciencedirect.com/science/article/pii/S2212827116007447

[26] A. H. Fritz, *Fertigungstechnik*. Berlin, Heidelberg: Springer Berlin Heidelberg, 2018.

[27] P. Minetola, F. Calignano, and M. Galati, "Comparing geometric tolerance capabilities of additive manufacturing systems for polymers," *Additive manufacturing*, vol. 32, p. 101103, 2020.

[28] L. Abdel-Malek and N. Asadathorn, "Process and design tolerance in relation to manufacturing cost: a review & extension," *The Engineering Economist*, vol. 40, no. 1, pp. 73–100, 1994.

[29] *Geometrical product specifications (GPS): ISO code system for tolerances on linear sizes*, ISO 286, 2010.

[30] *Schaeffler Technical Pocket Guide STT*, 3rd ed. Schaeffler Technologies AG & Co. KG, 2021. [Online]. Available: https://schaeffler-publications.com/stt-en-gb.html

[31] Y. Zhao, Y. Chen, and Y. Zhou, "Novel mechanical models of tensile strength and elastic property of FDM AM PLA materials: Experimental and theoretical analyses," *Materials & Design*, vol. 181, p. 108089, 2019.

[32] R. T. L. Ferreira, I. C. Amatte, T. A. Dutra, and D. Bürger, "Experimental characterization and micrography of 3D printed PLA and PLA reinforced with short carbon fibers," *Composites Part B: Engineering*, vol. 124, pp. 88–100, 2017. [Online]. Available: https://www.sciencedirect.com/science/article/pii/S135983681633195X

[33] Harmonic Drive AG, "Engineering Data HFUS-2A Component Sets." [Online]. Available: https://harmonicdrive.de/fileadmin/user_upload/2014_11_ED_1019658_HFUS-2A.pdf